

Measurement and prediction of geometric imperfections in structural stainless steel members

R. B. Cruise[†] and L. Gardner[‡]

*Department of Civil and Environmental Engineering, Imperial College London,
South Kensington Campus, London, SW7 2AZ, UK*

(Received December 20, 2005, Accepted April 24, 2006)

Abstract. Geometric imperfections have an important influence on the buckling response of structural components. This paper describes an experimental technique for determining imperfections in long (5.7 m) structural members using a series of overlapping measurements. Measurements were performed on 31 austenitic stainless steel sections formed from three different production routes: hot-rolling, cold-rolling and press-braking. Spectral analysis was carried out on the imperfections to obtain information on the periodic nature of the profiles. Two series were used to model the profile firstly the orthogonal cosine and sine functions in a classic Fourier transform and secondly a half sine series. Results were compared to the relevant tolerance standards. Simple predictive tools for both local and global imperfections have been developed to enable representative geometric imperfections to be incorporated into numerical models and design methods.

Keywords: geometric imperfections; stainless steel structures; Fourier series.

1. Introduction

The manufacture of structural members is carried out to specified tolerances. However, within these controlled geometric limits, imperfections exist that are directly attributable to the manner in which the sections were produced. Both the magnitude and distribution of these imperfections have an important influence on the load carrying capacity of structural members. Additional geometric imperfections or damage may also arise due to handling, storage and erection. These types of localised non-periodic imperfections (such as dents) are not well identified by the spectral analysis techniques implemented herein. Studies of the influence of localised imperfections on the structural performance of tubular members have been described by Pacheco and Durkin (1988) and Hambly and Calladine (1996). Other forms of production-related imperfections will also influence structural performance, such as material non-homogeneity and residual stresses; these are under consideration as part of a wider study.

The current study presents experimental results of detailed imperfection measurements made on austenitic stainless steel angles and hollow sections produced from three different production routes: hot-rolling and two types of cold-forming - cold-rolling and press-braking. A total of four hot-rolled

[†] Research Student, E-mail: Rachel.cruise@imperial.ac.uk

[‡] Lecturer, Corresponding author, E-mail: Leroy.gardner@imperial.ac.uk

angles, twenty press-braked angles and seven cold-rolled square and rectangular hollow sections were examined. An imperfection rig was constructed that allowed samples of up to 5.7 m in length to be measured. Results of this study may be used to define suitable imperfections for inclusion in numerical models and for the development of structural design guidance. Simple predictive models are proposed.

For structural stainless steel members there is a limited amount of published imperfection data. Measurements of local imperfections taken from short cold-rolled stainless steel stub columns and global imperfections taken from long column samples were reported by Gardner and Nethercot (2004). As part of structural testing programmes on stainless steel members, Liu and Young (2003), Rasmussen and Hancock (1993) and Talja and Salmi (1995) also present global imperfection measurements. A review of the structural use of stainless steel has been conducted by Gardner (2005).

Cases where detailed imperfection analyses and modelling has been carried out are typically for structural components that are known to be sensitive to the existence of initial imperfections. One such area is in shell structures where the ability to characterise initial imperfections has a very direct effect on the accuracy of predicting the load carrying capacity. To this end imperfection data banks were set up to collate the experimental data; this development is detailed by Singer and Abramovich (1995).

Spectral analysis has been performed in previous research on imperfection measurements for two reasons, firstly to identify periodic patterns in the profiles and secondly in order to generate representative imperfection profiles that can be used in finite element models. Use of the classic Fourier transform fits to a series of cosine and sine functions to a given profile. This technique is based on the Fourier theorem (Bracewell 1986) and has been employed, for example, by Berry *et al.* (2000) for the analysis of imperfections in steel cylinders and Teng *et al.* (2005) used a two dimensional Fourier analysis on steel silos. Schafer and Peköz (1998) also used the Fourier transform for the analysis of imperfection data from cold-formed steel lipped channel sections and proposed a probabilistic method to generate artificial imperfection profiles from experimental spectra for application in finite element models. Probabilistic methods of introducing imperfections have been implemented by Dubina and Ungureanu (2002) in finite element simulations of carbon steel channel and hat sections and used by Chryssanthopoulos and Poggi (1995) to map imperfections in other types of components such as composite panels.

An alternative to modelling an imperfection profile as a classic Fourier series, is to use the least squared method to fit a series of half sine waves. This technique allows direct correlation with global buckling modes and has been successfully employed by Bernard *et al.* (1999), and Wheeler and Pircher (2002). The technique had previously been used to identify chemical elements with in pulse height spectra (Trombka and Schmadeberk 1970, Haaland and Thomas 1988). Chryssanthopoulos *et al.* (1991), Lechner and Pircher (2005) and Hearn and Metcalfe (1995) discuss the Fourier and least squared method for fitting alternative functions.

Sensitivity to imperfections in structural members depends upon material properties, loading arrangement and the local and global geometric proportions (slenderness) of the cross-section and member. Typically global imperfections are considered as a fixed proportion of the member length L , whilst local imperfections are related to the thickness or local slenderness of the section. Finite element models presented by Chou *et al.* (2000), and Kaitila (2002), Gardner and Nethercot (2004) demonstrate an established method of including imperfections by introducing global and local eigenmodes of representative amplitudes.

Both the classical Fourier transform and the least squared technique are employed in the present study to model imperfection data collected through an experimental programme. The resulting spectral peaks are used to develop simple models for global and local imperfections amplitudes.

2. Modelling precedents

Extensive research has been carried out on the influence of imperfections on cold-formed carbon steel structural members. A number of predictive models have been developed to estimate the magnitude of the local imperfections ω_o , such as those presented by Dawson and Walker (1972). Within their paper three models were considered. Firstly a simple model which relates the amplitude to the section's thickness t is given in Eq. (1).

$$\omega_o = 0.2t \quad (1)$$

Two more sophisticated expressions were proposed (Eqs. (2) and (3)) both of which include the ratio of yield strength σ_y to elastic critical buckling stress σ_{cr} , representing the slenderness of the plate. The value of the coefficients α and β were derived from experimental data.

$$\frac{\omega_o}{t} = \alpha \left(\frac{\sigma_y}{\sigma_{cr}} \right) \quad (2)$$

$$\frac{\omega_o}{t} = \beta \left(\frac{\sigma_y}{\sigma_{cr}} \right)^{0.5} \quad (3)$$

Gardner and Nethercot (2004) determined values for the α and β coefficients for cold-rolled stainless steel hollow sections based on imperfection measurements of short samples. Values of $\alpha = 0.023$ and $\beta = 7.3 \times 10^{-6}$ were proposed. The yield strength σ_y was taken as the 0.2% proof strength $\sigma_{0.2}$ due to the rounded nature of the stainless steel stress-strain curve. Eq. (2) was found to best represent the experimental data.

Schafer and Peköz (1998) proposed expressions for local imperfections which differentiated between internal elements ω_1 and outstand elements ω_2 and elements in cold-formed sections. For internal elements, Eq. (4) (based on plate width d) and Eq. (5) (based on plate thickness t) were proposed.

$$\omega_1 = 0.006d \quad (4)$$

$$\omega_1 = 6te^{-2t} \quad (5)$$

For outstand elements, Eq. (6) was proposed to estimate the local imperfection ω_2

$$\omega_2 \approx t \quad (6)$$

Geometric tolerances for structural sections are controlled by a number of Standards. The European Standard EN 10162 (2003) defines the tolerances for cold-rolled hollow sections. Global imperfections are defined as 'the deviation from straight' and for square hollow sections a tolerance

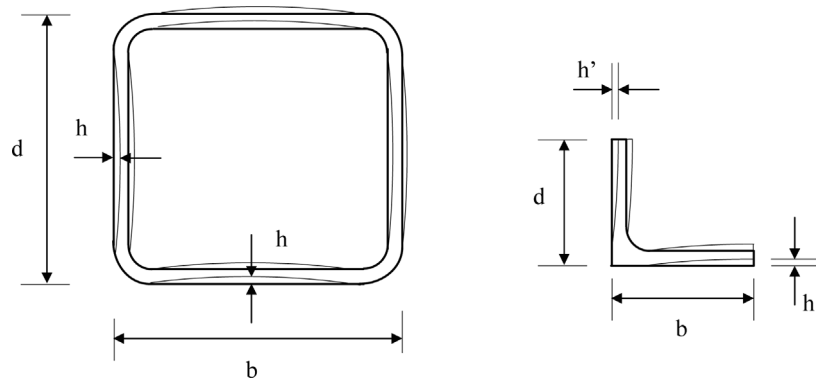


Fig. 1 (a) Convexity and concavity of box sections h , (b) Deviation from square of angle flanges, h'

of $0.002 L$, where L is the length of the member, is specified. Concavity and convexity of internal elements, h (Fig. 1a) should not exceed $0.008d$ or $0.008b$, where d and b are the plate widths, and should be less than an absolute value of 0.5 mm.

Tolerances for hot-rolled angles are set out in EN 10056-2 (1993). EN 10056-2 is principally for hot-rolled carbon steel angles, and in fact states that it is not applicable for stainless steel sections. However, Annex C of EN 10088-3 (2005), the material code for stainless steels refers explicitly to EN 10056-2 (1993) as the only relevant Code and as the Standard used by manufacturers. For equal angles, of flange width less than 150 mm, the specified tolerance on deviation from straight is $0.004 L$, whilst on out of squareness h' (Fig. 1b) an absolute tolerance of 1 mm is specified. EN 10162 (2003) explicitly states that it does not cover press-braked sections, and no other suitable Standard has been determined.

3. Imperfection measurements

3.1 Specimens

The specimens investigated in this research programme were formed by three different production processes: hot-rolling, cold-rolling and press-braking. A summary of the specimens is given in Table 1. An identification system has been adopted whereby PB, HR and CR (appended by a number in the case of multiple specimens of the same nominal dimensions) denote press-braked, hot-rolled and cold-rolled sections respectively. This is followed by section size ($b \times d \times t$), and where relevant, the internal corner radii r_i .

Cold-rolling and press-braking are both types of cold-forming where sheet stainless steel is formed at room temperature by plastic deformation. Cold-rolling is a continuous process using strip material that is firstly de-coiled and then passed through a sequential set of rolls which gradually form the section shape. For closed sections an automatic seam weld completes the section. Press-braking is a more manual process often used for smaller batches of simple sections. The coil material is firstly de-coiled and slit to appropriate dimensions before being placed between a tool and die in a press-brake to create simple open sections. The properties of the final cross-sections will be related to both the cold-forming process (cold-rolling or press-braking) and the process by

Table 1 Nominal dimensions of specimens

Specimen identification	<i>b</i> (mm)	<i>d</i> (mm)	<i>t</i> (mm)	<i>r_i</i> (mm)	<i>L</i> (m)
Press-braked equal angles					
PB1 50×50×2 (<i>r_i</i> = 1.7)	50	50	2	1.7	2.0
PB2 50×50×2 (<i>r_i</i> = 1.7)	50	50	2	1.7	2.0
PB3 50×50×2 (<i>r_i</i> = 1.7)	50	50	2	1.7	2.0
PB1 50×50×2 (<i>r_i</i> = 3.2)	50	50	2	3.2	2.0
PB2 50×50×2 (<i>r_i</i> = 3.2)	50	50	2	3.2	2.0
PB 50×50×2 (<i>r_i</i> = 3.5)	50	50	2	3.5	2.5
PB 50×50×2 (<i>r_i</i> = 4.5)	50	50	2	4.5	2.5
PB 50×50×2 (<i>r_i</i> = 7.5)	50	50	2	7.5	2.5
PB1 50×50×3 (<i>r_i</i> = 3.2)	50	50	3	3.2	2.0
PB2 50×50×3 (<i>r_i</i> = 3.2)	50	50	3	3.2	2.0
PB 50×50×3 (<i>r_i</i> = 3.5)	50	50	3	3.5	2.5
PB 50×50×3 (<i>r_i</i> = 4.5)	50	50	3	4.5	2.5
PB 50×50×3 (<i>r_i</i> = 7.5)	50	50	3	7.5	2.5
PB 50×50×4 (<i>r_i</i> = 3.5)	50	50	4	3.5	2.5
PB 50×50×4 (<i>r_i</i> = 4.5)	50	50	4	4.5	2.5
PB 50×50×4 (<i>r_i</i> = 7.5)	50	50	4	7.5	2.5
PB 50×50×5 (<i>r_i</i> = 3.5)	50	50	5	3.5	2.5
PB 50×50×5 (<i>r_i</i> = 4.5)	50	50	5	4.5	2.5
PB 50×50×5 (<i>r_i</i> = 7.5)	50	50	5	7.5	2.5
PB 50×50×6 (<i>r_i</i> = 7.5)	50	50	6	7.5	2.5
Hot-rolled equal angles					
HR 50×50×3	50	50	3	-	6.0
HR 50×50×5	50	50	5	-	6.0
HR 50×50×6	50	50	6	-	6.0
HR 50×50×10	50	50	10	-	6.0
Cold-rolled SHS/RHS					
CR 100×50×2	100	50	2	-	6.0
CR 100×100×2	100	100	2	-	6.0
CR 100×50×3	100	50	3	-	6.0
CR 100×100×3	100	100	3	-	6.0
CR 100×50×4	100	50	4	-	6.0
CR 100×100×4	100	100	4	-	6.0
CR 100×50×6	100	50	6	-	6.0

which the coil material was formed. Generally, for thicknesses of 2 mm or less the coil material is cold-rolled (cold-reduced), whilst for thicknesses greater than 2 mm coil material is hot-rolled.

Hot-rolled sections are formed either from billets produced from a continuous caster that are

subsequently re-heated, or directly through continuous casting. In the continuous casting process, hot material passes through a series of rolls that gradually shape the required section. The sections are then cooled and in some cases annealed (softened) to reduce residual stresses. Sections may also be straightened by gaging or rolling.

3.2 Experimental technique

Imperfection measurements are commonly taken on short sample lengths due to the size restrictions imposed by measurement equipment. For example imperfection measurements reported on carbon steel structural sections have been taken with coordinate measuring machines, as the general technique adopted by the manufacturers. A more readily available alternative uses a mill bed to lay the sample on and a differential transformer is moved along the surface of a sample, taking measurements at intervals. This technique was adopted by Schafer and Peköz (1998). Both techniques use a flat surface as a reference plane from which measurements are taken.

Spectral imperfection analyses carried out on carbon sections have indicated that the significant peaks tend to occur at the lower frequency values (Wheeler and Pircher 2003). Measurements taken over longer samples therefore allow more detailed information on the low frequency wavelengths, which relate to the global imperfections present in structural members.

To measure imperfections in samples over longer lengths, a technique of overlapping measurements was employed in order to identify and remove the imperfections in the test setup itself, so that the true surface profile of the sample could be mapped. Similar techniques have been successfully used to measure imperfections in steel silos (Ding *et al.* 1996), large cylinders (Wheeler and Pircher 2002).

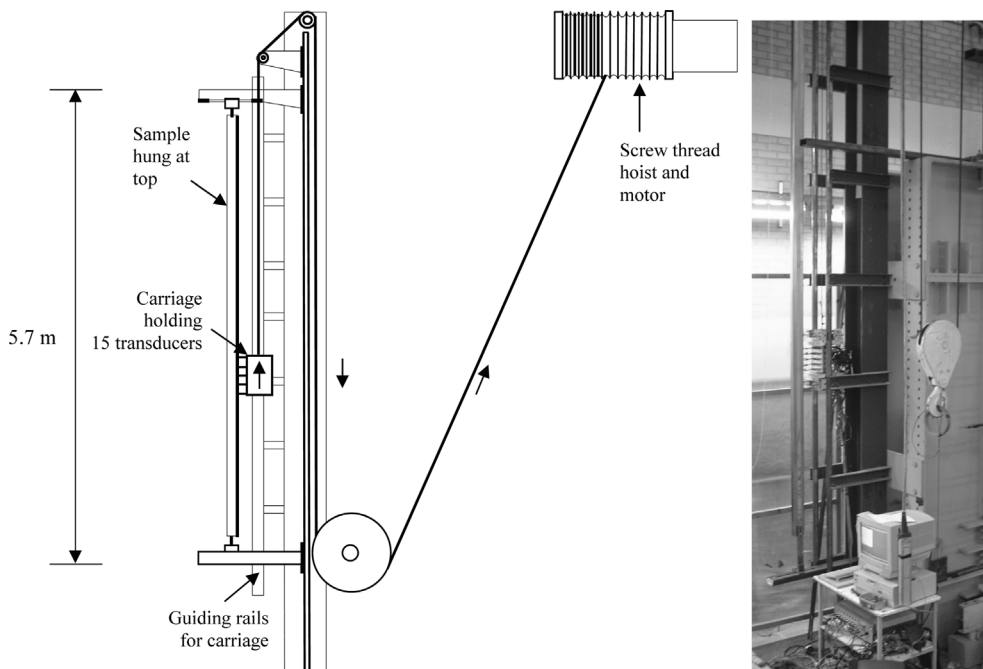


Fig. 2 Arrangement of the imperfection rig

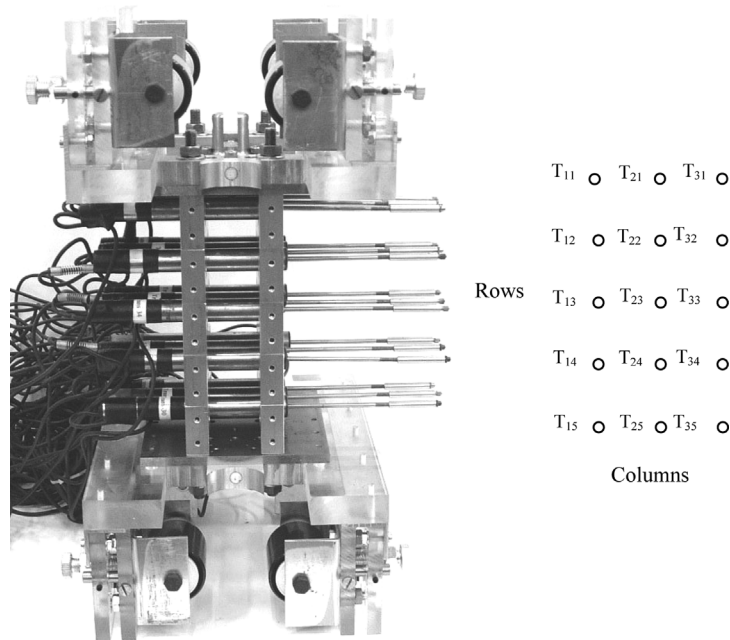


Fig. 3 Carriage and transducer arrangement

The experimental setup employed in the present study comprised a carriage holding an array of three by five spring-loaded linear voltage displacement transducers located on two vertical guiding rails. The carriage was driven along the guide rails at a constant speed by a pulley hoist. The specimen lengths measured up to 5.7 m and were hung adjacent to the guide rails, as shown in Fig. 2.

Data was recorded at one second intervals. This equated to measurements taken at 6.7 mm intervals along the length of the sample. The fifteen transducers were arranged in five rows and three columns, as shown in Fig. 3. The transducers operated to an accuracy of ± 0.01 mm. This enabled five overlapping measurements to be made at three locations on the faces of the cross-sections. The numbering system shown in Fig. 3 identifies the column C and row R of each transducer respectively. The data was recorded using the Dalite software package and processed in MatLab.

The overall geometric shape of the two guiding rails was measured using an optical theodolite. The measurements showed that the guiding rails were within 1 mm of being absolutely straight. These global deviations of the imperfection rig were directly subtracted from the imperfection profile of the specimens. Local imperfections in the rig were removed using overlapping readings, as discussed in the following section. Nylon plastic tips of 10 mm diameter were affixed to the transducers to minimise friction with the specimens, and to ensure contact was maintained when taking edge readings on specimens that were imperfect perpendicular to the measurement direction. The transducers were spring-loaded to maintain contact with the sample. The resulting lateral force from the springs caused the sample to deflect. In order to eliminate this deflection the readings from the transducers were combined with measurements taken with a class IEC 825 laser, which had the accuracy quoted by the manufacturers of ± 0.125 mm. This accuracy was however stated for use on a white surface. The metallic shine of the samples affected the accuracy of the laser and a reduced

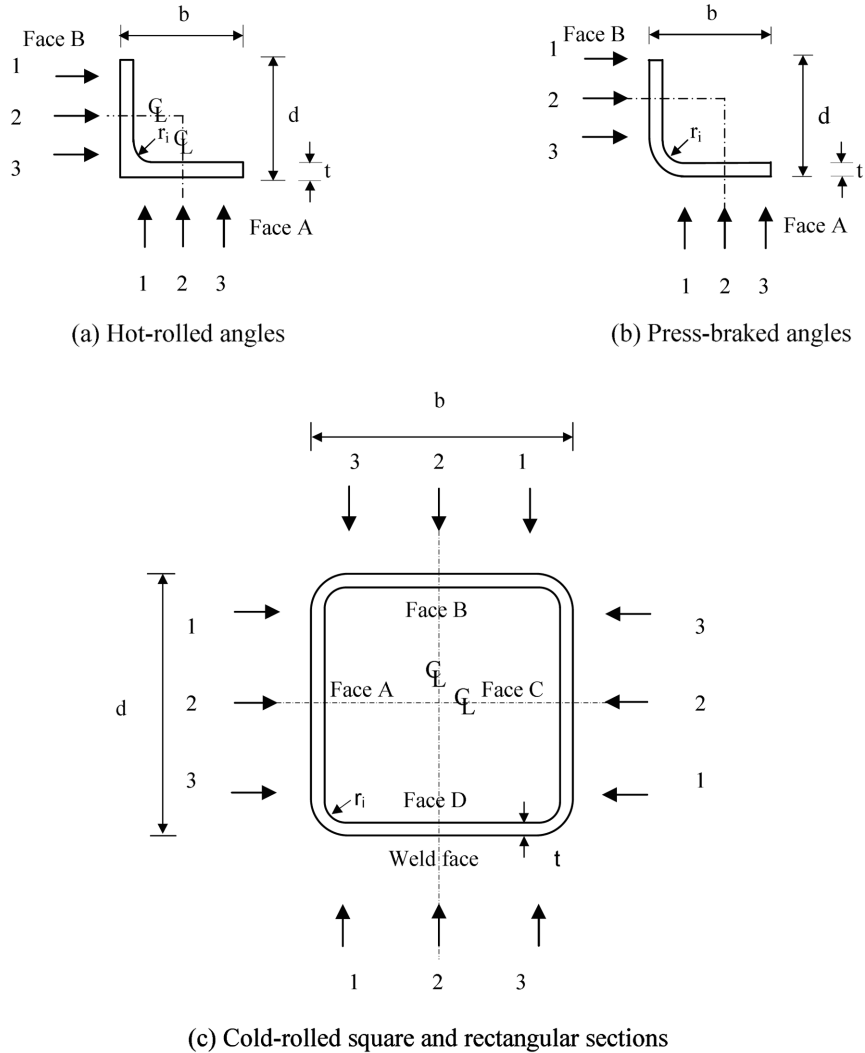


Fig. 4 Location of imperfection measurements for the different types of sections

accuracy of ± 0.3 mm was estimated. Readings were taken in the three positions measured by the three columns of transducers. For the different types of sections the location of the three sets of readings on each face varied. The positions of the readings taken are shown in Fig. 4.

3.3 Data processing

In order to compile a profile of accuracy of ± 0.01 mm and remove the deflection caused by the sprung loaded transducers, the measurements taken by the laser and the transducer were combined. The global shape of the profile was taken from the laser reading and smaller imperfections were taken from the more sensitive transducer readings. An example of a set of recorded data is shown in

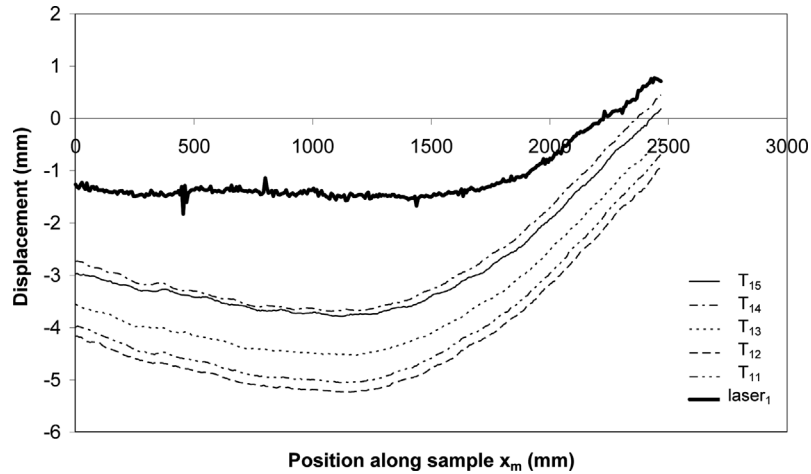


Fig. 5 Individual readings for transducers in column 1 (T_{11} to T_{15}) and the corresponding laser reading $laser_1$

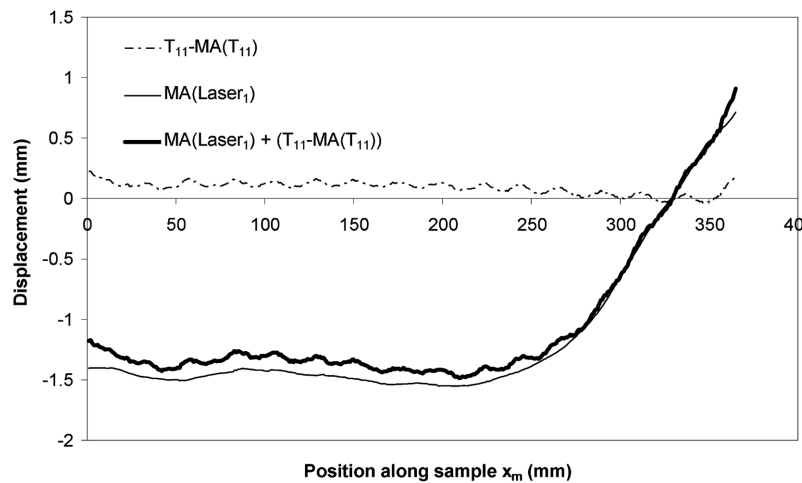


Fig. 6 Moving average of the laser reading $MA(laser_1)$, the reduced transducer reading $T_{11} - MA(T_{11})$ and the combined profile $MA(laser_1) + (T_{11} - MA(T_{11}))$

Fig. 5. In order to compile a profile for each of the three locations the following procedure was followed.

A moving average ($MA(laser_c)$) of 30 data points was determined to isolate the global shape, of the imperfection data from the noise generated below the level of accuracy of the laser. To combine the transducer measurements with this global shape, moving averages were taken for each transducer reading ($MA(T_{CR})$), again removing any variations below 0.3 mm. Subtracting the reduced transducer reading from the complete transducer reading yielded the transducer measurements below the level of accuracy of the laser ($T_{CR} - MA(T_{CR})$). Finally, superimposing the global imperfection shape from the laser and these finer measurements from the transducers gave five profiles for each measurement location, without the deflection caused by the lateral force of the transducers. A graphical example of this process is shown in Fig. 6.

Each displacement profile P_{CR} (where C and R denote the column and row, respectively of the transducer) was related to the others by offsetting them according to readings taken at constant displacement, as given by Eq. (7).

$$P_{CR} = MA(laser_C) + (T_{CR} - MA(T_{CR})) - offset_{CR} \quad (7)$$

The five overlapping measurements for each location were used to remove the local imperfections in the rig itself from the measured readings. Fig. 7 illustrates that the five transducers in a column sequentially measure the same point whilst obtaining a different reading caused by the imperfect guiding rails. Due to the orientation of the carriage, the rig imperfections were expected to be the

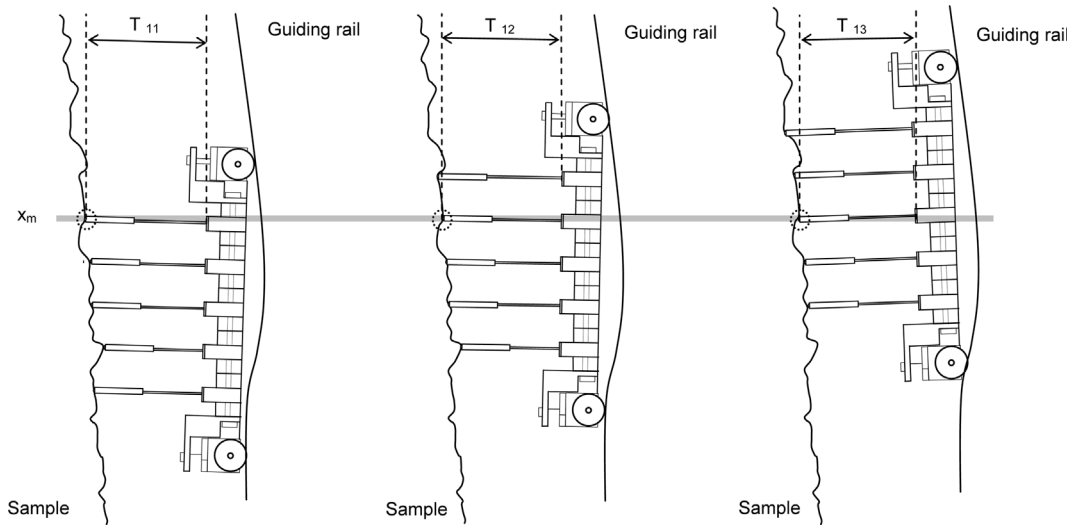


Fig. 7 Creation of profile differences due to the imperfections of the guiding rail

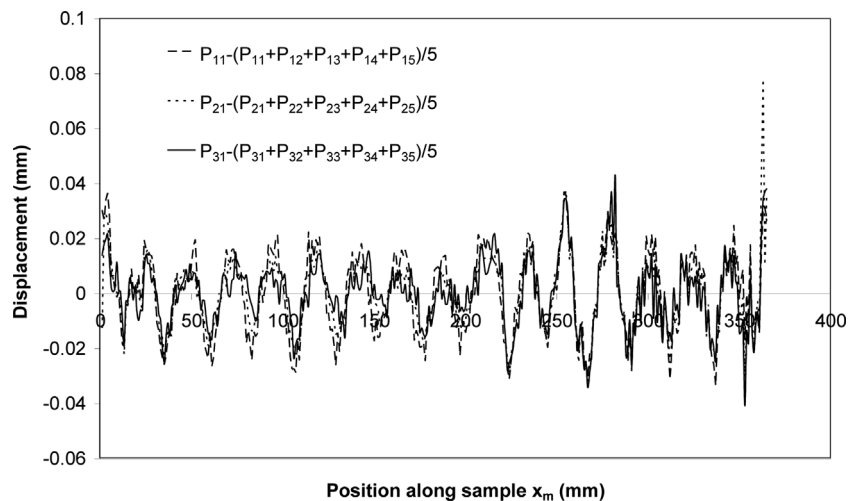


Fig. 8 Correlation between profile differences found for the first row of transducers (T_{11} to T_{31})

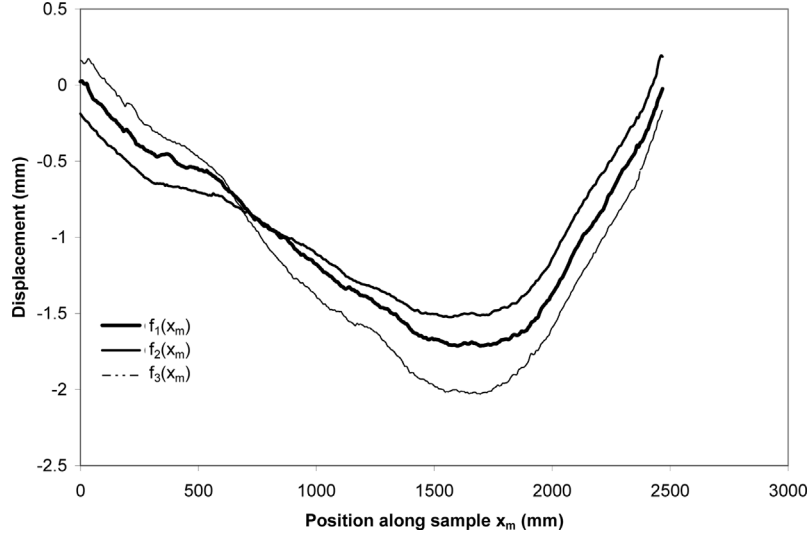


Fig. 9 Related profiles $f_1(x_m)$, $f_2(x_m)$, and $f_3(x_m)$ which are located at the corner, centre and edge of the outstand flange of a press-braked angle section

same for transducers in the same row. Profile differences determined by subtracting the individual transducers readings from an average of the transducer readings in the same column (Eqs. (8) and (9)) showed excellent correlation as illustrated in Fig. 8.

$$P_{1R} - ((P_{11} + P_{12} + P_{13} + P_{14} + P_{15})/5) \approx P_{2R} - ((P_{21} + P_{22} + P_{23} + P_{24} + P_{25})/5) \quad (8)$$

$$P_{1R} - ((P_{11} + P_{12} + P_{13} + P_{14} + P_{15})/5) \approx P_{3R} - ((P_{31} + P_{32} + P_{33} + P_{34} + P_{35})/5) \quad (9)$$

Making the assumption that, due to the length of the trolley compared to the magnitude of the rig imperfections, the change in angle between the carriage and the global shape of the guide rails is small, a small angle approximation is made and the identified profile differences are defined as the local imperfections of the rig. Since rig imperfections that move the transducers towards the sample will cause a decrease in any transducer reading and imperfections that move the transducer away from the sample will give the reverse effect, the average profile differences from the three transducers in each row were then added to the individual profiles P_{CR} . This process is described by Eq. (10) to give the corrected profiles $f_{CR}(x_m)$, where x_m is the location x along the specimen length at discrete data point m .

$$f_{CR}(x_m) = P_{CR} + ((P_{1R} - ((P_{11} + P_{12} + P_{13} + P_{14} + P_{15})/5)) + (P_{2R} - ((P_{21} + P_{22} + P_{23} + P_{24} + P_{25})/5)) + (P_{3R} - ((P_{31} + P_{32} + P_{33} + P_{34} + P_{35})/5)))/3 \quad (10)$$

These corrected profiles were averaged to provide a single profile for each of the three measurement locations on the specimen faces (Eq. (11)).

$$f_C(x_m) = (f_{C1}(x_m) + f_{C2}(x_m) + f_{C3}(x_m) + f_{C4}(x_m) + f_{C5}(x_m))/5 \quad (11)$$

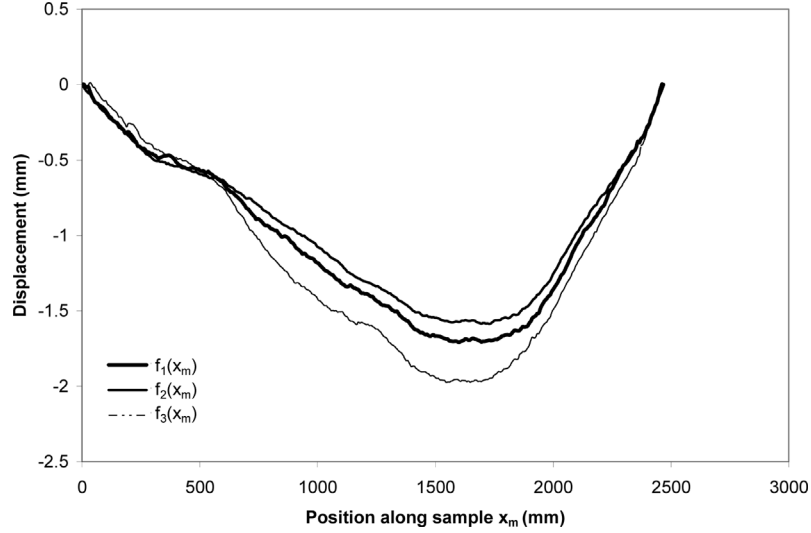


Fig. 10 Unrelated profiles $f_1(x_m)$, $f_2(x_m)$, and $f_3(x_m)$ which are located at the corner, centre and edge of the outstand flange of a press-braked angle section

The profiles were related to a common datum; resulting profiles for a press-braked sample are shown in Fig. 9. The profiles for each of the three measurement locations may also be considered as unrelated on a datum comprising a straight line between the ends of the profiles, as shown in Fig. 10. For the cold-rolled sections it was observed that each end of the centre profile flared outwards. This was also observed by Gardner and Nethercot (2004) and is believed to be due to the release of bending residual stresses that were induced during production. In order for these not to influence the spectral analysis, 1% of the length was removed at either end of the cold-rolled specimen profiles.

4. Data analysis

This section sets out two principal techniques of obtaining spectral information from the collected imperfection measurements: the classic Fourier transform and the least squared method for half sine waves. Both techniques were used to analyse the related and the unrelated imperfection data.

The Fourier theorem states that the sum of odd and even functions in an infinite series can precisely model any continuous function. Therefore an imperfection function $f_c(x)$, where \bar{x} is a position along the sample normalised against the sample length, can be expressed as the sum of cosine and sine functions of different frequencies as given by Eq. (12).

$$f_c(\bar{x}) = \sum_{n=0}^{\infty} a_n \cos(n2\pi\bar{x}) + \sum_{n=0}^{\infty} b_n \sin(n2\pi\bar{x}) \quad (12)$$

The frequency of each sinusoidal function is represented by an integer value n , which is the number of wavelengths within the imperfection function. The coefficients or amplitudes of the cosine and sine functions are a_n and b_n respectively.

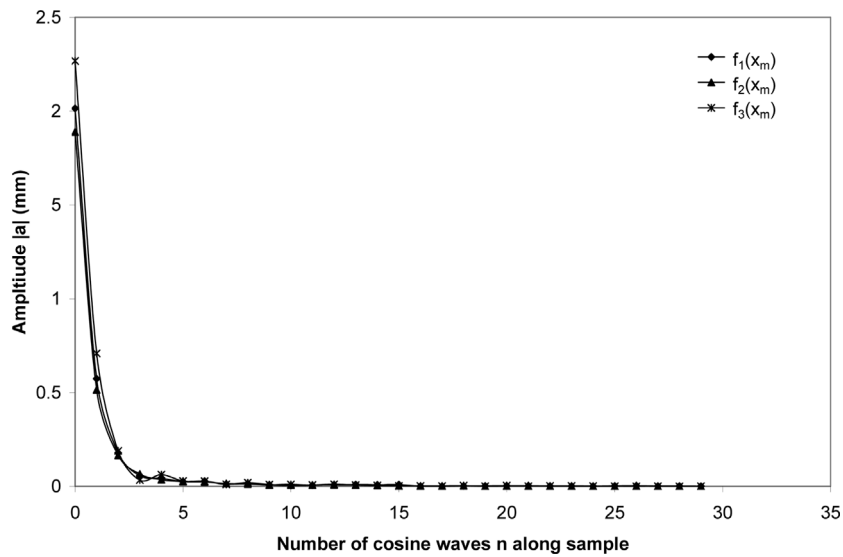


Fig. 11 Real (cosine) coefficients for $f_1(x_m)$, $f_2(x_m)$, and $f_3(x_m)$ which are located at the corner, centre and edge of the outstand flange of a press-braked angle section

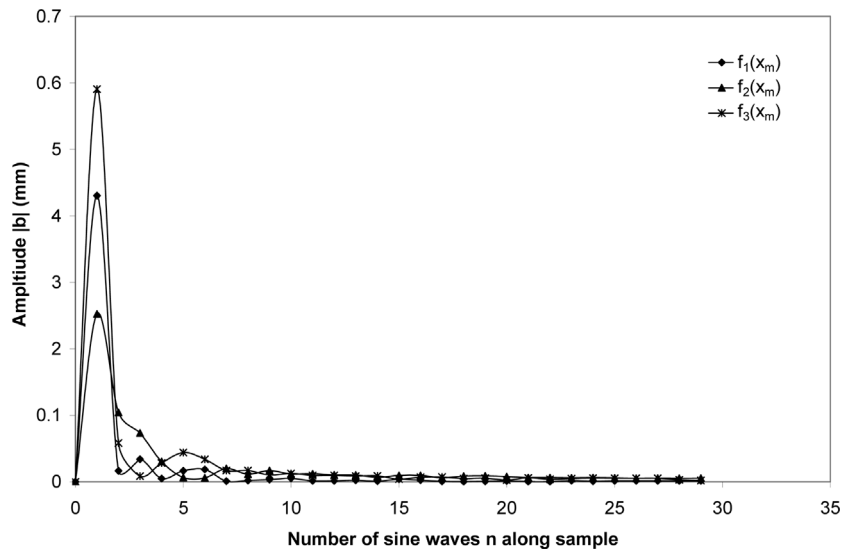


Fig. 12 Imaginary (sine) coefficients for $f_1(x_m)$, $f_2(x_m)$, and $f_3(x_m)$ which are located at the corner, centre and edge of the outstand flange of a press-braked angle section

In practical situations with a discrete set of data the frequency spectrum is limited by the Nyquist frequency N which is half the number of discrete data points. For the discrete case, the inverse of the Fourier transform still produces an exact model of the imperfection function because the highest frequency that can be detected (the Nyquist frequency N) is determined by the intervals at which the readings are taken. The modulus of the real coefficients and the imaginary coefficients are plotted separately in Figs. 11 and 12 respectively. Fig. 13 shows the combined spectral coefficient.

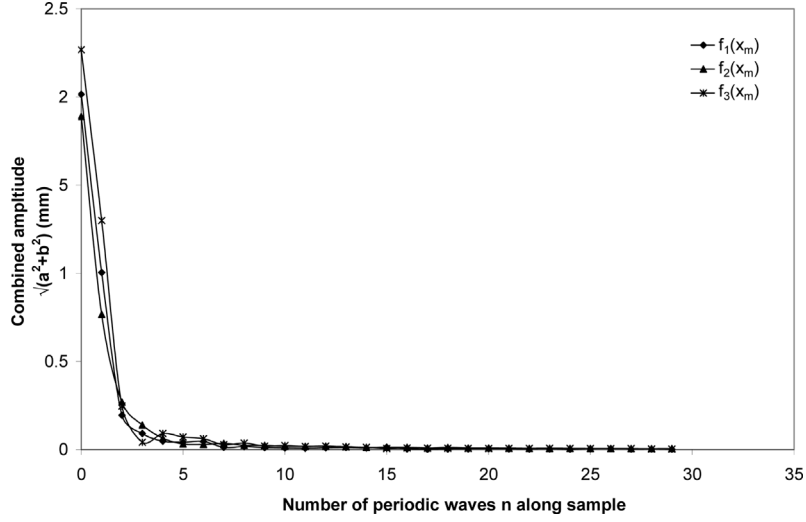


Fig. 13 Combined imaginary and real coefficients for $f_1(x_m)$, $f_2(x_m)$, and $f_3(x_m)$ which are located at the corner, centre and edge of the outstand flange of a press-braked angle section

The least squared approach models the imperfection function as the sum of a linear function and a series of ($n = 1$ to $n = N$) half sine functions as stated by Eq. (13). This approach is summarised below and has been discussed in more detail by Bernard *et al.* (1999). Eq. (13) is presented in terms of a normalised longitudinal position \bar{x}_m , given in Eq. (14), where x_m is the location x along the specimen length for the discrete data point m , x_1 is the location of the initial data point, δ is an offset value and L is the specimen length. Since the half sine functions are not independent, the modelling function $f_C'(\bar{x}_m)$ will not be exact and will always exhibit a difference from the experimental imperfection function $f_C(\bar{x}_m)$. A process of minimising the resultant modelling error $\{V\}$ of the spectral peaks is carried out by varying the offset value δ of the half sine series from the origin of the data.

$$f_C'(\bar{x}_m) = c_1 + c_2 \bar{x}_m + \sum_{n=1}^N c_{n+2} n \sin \pi \bar{x}_m \quad (13)$$

$$\bar{x}_m = \left(\frac{x_m - x_1 - \delta}{L} \right) \quad (14)$$

Converting the notation to matrices, the design matrix $[A]$ contains the function series and $\{w\}$ contains the imperfection readings w_1 to w_M , as shown in Eqs. (15) and (16), where M is the number of discrete data points. The spectral coefficients are given as $\{c\}$, defined in Eq. (17), and the error between the experimental imperfection function and the modelling function is given as a vector $\{V\}$, which is defined in Eq. (18).

$$[A] = \begin{bmatrix} 1 & \bar{x}_1 & \sin \pi \bar{x}_1 & \dots & N \sin \pi \bar{x}_1 \\ 1 & \bar{x}_2 & \sin \pi \bar{x}_2 & \dots & N \sin \pi \bar{x}_2 \\ \vdots & \vdots & \vdots & \vdots & \vdots \\ 1 & \bar{x}_M & \sin \pi \bar{x}_M & \dots & N \sin \pi \bar{x}_M \end{bmatrix} \quad (15)$$

$$\{w\} = \begin{Bmatrix} w_1 \\ \vdots \\ w_M \end{Bmatrix} \quad (16)$$

$$\{c\} = \begin{Bmatrix} c_1 \\ c_2 \\ \vdots \\ c_{N+2} \end{Bmatrix} \quad (17)$$

$$\{V\} = \{w\} - [A]\{c\} \quad (18)$$

In order to estimate the variance in the spectral coefficients, the experimental error or the variance of each individual measurement is introduced in a weighting matrix $[G]$ (Eq. (19)). Since the experimental error of each data point taken by the transducers was estimated as ± 0.01 mm, σ_1^2 to σ_M^2 have been taken as the same value.

$$[G] = \begin{bmatrix} \frac{1}{\sigma_1^2} & & & \\ & \frac{1}{\sigma_2^2} & & \\ & & \ddots & \\ & & & \frac{1}{\sigma_M^2} \end{bmatrix} \quad (19)$$

The vector $\{c\}$ containing the least squared spectral coefficients is calculated from Eq. (20):

$$\{c\} = ([A]^T [G] [A])^{-1} [A]^T [G] \{w\} \quad (20)$$

The variance σ_{an}^2 associated with the each spectral coefficient in $\{c\}$ can be calculated from Eq. (21), where $\hat{\sigma}_0^2$ is the variance factor (Eq. (23)) and Q_{ii} are the diagonal values of the covariance matrix $[Q]$ (Eq. (22)). Employing a normal distribution with a confidence level of 99.5% the confidence levels for the peaks are found by multiplying σ_{an}^2 by 2.58. This confidence level defines a magnitude of the spectral peaks below which it is uncertain whether the peaks relate to the data or have been generated by experimental and modelling errors.

$$\sigma_{an}^2 = \hat{\sigma}_0^2 Q_{ii} \quad (21)$$

$$[Q] = ([A]^T [G] [A])^{-1} \quad (22)$$

The ratio of the square of the modelling error to the experimental error of each data point is termed the variance factor $\hat{\sigma}_0^2$ which is calculated by Eq. (23). Using a chi squared distribution with r degrees of freedom when the variance factor equals one i.e., when the modelling error equals the experimental error, the model is said to be a good fit to the experimental data. The number of degrees of freedom r is expressed by Eq. (24).

$$\hat{\sigma}_0^2 = \frac{\{V\}^T [G] \{V\}}{r} \quad (23)$$

$$r = M - (N + 2) \quad (24)$$

In cases where the variance factor is not equal to unity, the assumed experimental error can be revised until the variance factor does equal unity, providing an estimated experimental error $\bar{\sigma}$. To find the best fit, the lowest value of the variance factor was sought whilst varying the offset value δ . Due to the asymmetrical nature of the half sine wave function the offset value δ was varied from -1 to 1 . A common minimum variance factor was found for the three profiles taken from each section face. The offset values were found to occur repeatedly around values -1 , 0 and 1 due to the significance of the first half sine wave in the imperfection profiles.

With the introduction of the offset into the analysis both the related and unrelated profiles can become discontinuous functions if the offset is not equal to -1 or 1 . Profile functions with discontinuities caused large alternating positive and negative least squared coefficients and high variance values to be observed. These high variance values are also seen in the Gibbs phenomenon, discussed by Bracewell (1986). The Gibbs phenomenon is observed as ringing close to discontinuities in a function and it is caused by forming the profile from a truncated Fourier series thereby removing large amplitude high frequency terms that are required to fully describe the profile discontinuity. In order to remove the profile discontinuity and thereby reduce the variance of the imperfection data a method of tapering was employed. Priestley (1992) discusses typical tapering functions that can be employed. A hermite interpolation curve, described in Prenter (1975), was employed to generate five data points before the beginning of the profile and five data points afterwards, to taper the function and ensure the continuity between the beginning and the end of the imperfection function. An example of a least squared spectrum for three corresponding profiles is shown in Fig. 14. The prediction error sum of squares or PRESS (Lechner and Pircher 2005) was determined for least squared half sine wave coefficients to determine the significance of the individual component coefficients.

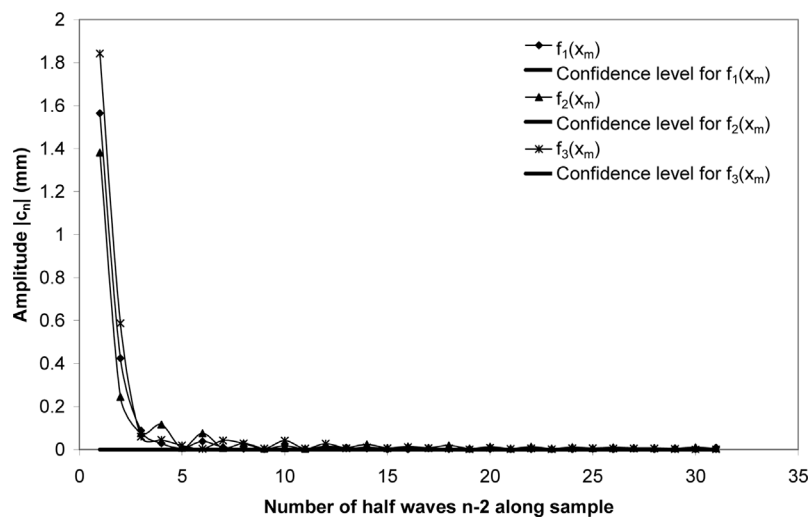


Fig. 14 Least squared coefficients and their confidence levels

Table 2 Data for press-braked samples

Specimen identification	t (mm)	r_i (mm)	L (mm)	$ a_0 $ (mm)	$ c_3 $ (mm)	$2.54\sigma_{a3}^2$ (mm)	δ/L (mm)	$\bar{\sigma}$ (mm)	ω_o ($\zeta=1$) (mm)	ω_o ($\zeta=10$) (mm)
PB1 50×50×2 ($r_i = 1.7$)										
Face A	1.99	2.35	1986	0.11	0.04	1.93×10^{-5}	-0.0008	4.61×10^{-3}	0.03	0.60
Face B	1.99	2.35	1993	0.55	0.42	8.92×10^{-5}	-0.0032	2.93×10^{-3}	0.04	0.25
PB2 50×50×2 ($r_i = 1.7$)										
Face A	2.00	2.25	1993	0.08	0.03	1.11×10^{-3}	0.0056	4.03×10^{-3}	0.04	0.77
Face B	2.00	2.25	1980	0.12	0.00	1.54×10^{-5}	0.9988	3.73×10^{-3}	0.05	0.23
PB3 50×50×2 ($r_i = 1.7$)										
Face A	2.00	2.25	1993	0.11	0.06	1.50×10^{-5}	0.0004	4.33×10^{-3}	0.02	0.75
Face B	2.00	2.25	1986	0.38	0.17	5.06×10^{-5}	0.9976	4.33×10^{-3}	0.03	0.24
PB1 50×50×2 ($r_i = 3.2$)										
Face A	1.99	2.35	1986	0.50	0.38	2.03×10^{-5}	0.9984	3.78×10^{-3}	0.03	0.17
Face B	1.99	2.35	1993	0.49	0.35	5.69×10^{-5}	-0.9968	3.14×10^{-3}	0.03	0.14
PB2 50×50×2 ($r_i = 3.2$)										
Face A	2.02	4.50	1980	2.07	1.55	4.95×10^{-3}	0.0064	5.70×10^{-3}	0.03	0.14
Face B	2.02	4.50	1993	2.39	1.76	3.36×10^{-5}	-0.9988	5.50×10^{-3}	0.02	0.14
PB 50×50×2 ($r_i = 3.5$)										
Face A	1.95	4.33	2468	2.03	1.56	1.31×10^{-5}	-0.0012	3.15×10^{-3}	0.03	0.16
Face B	1.95	4.33	2475	0.06	0.13	3.39×10^{-3}	0.0056	3.59×10^{-3}	0.03	0.20
PB 50×50×2 ($r_i = 4.5$)										
Face A	1.98	5.50	2481	3.34	2.50	5.80×10^{-5}	0.0016	5.52×10^{-3}	0.03	0.11
Face B	1.98	5.50	2475	2.89	2.30	2.19×10^{-5}	-0.0012	4.08×10^{-3}	0.02	0.14
PB 50×50×2 ($r_i = 7.5$)										
Face A	1.98	8.00	2481	0.07	0.50	1.15×10^{-4}	0.9992	1.08×10^{-2}	0.03	0.23
Face B	1.98	8.00	2488	1.75	1.54	2.72×10^{-5}	-0.0004	5.77×10^{-3}	0.01	0.38
PB1 50×50×3 ($r_i = 3.2$)										
Face A	2.98	4.50	1993	1.51	1.17	2.06×10^{-3}	0.0056	5.50×10^{-3}	0.06	0.25
Face B	2.98	4.50	1993	1.17	0.93	2.45×10^{-3}	-0.9944	6.00×10^{-3}	0.06	0.08
PB2 50×50×3 ($r_i = 3.2$)										
Face A	2.99	4.50	1986	1.15	0.91	1.90×10^{-3}	0.9992	4.58×10^{-3}	0.02	0.12
Face B	2.99	4.50	1986	1.80	1.37	7.30×10^{-3}	-0.0008	2.84×10^{-3}	0.02	0.13
PB 50×50×3 ($r_i = 3.5$)										
Face A	2.98	3.50	2475	2.82	2.22	2.01×10^{-5}	0.9980	2.65×10^{-3}	0.02	0.18
Face B	2.98	3.50	2475	4.00	3.07	4.22×10^{-5}	-0.0012	5.67×10^{-3}	0.02	0.14
PB 50×50×3 ($r_i = 4.5$)										
Face A	2.97	4.67	2481	1.98	1.54	1.24×10^{-5}	0.9984	2.56×10^{-3}	0.01	0.12
Face B	2.97	4.67	2475	2.44	1.86	7.91×10^{-6}	-0.0008	2.83×10^{-3}	0.00	0.18
PB 50×50×3 ($r_i = 7.5$)										
Face A	2.98	7.50	2488	1.79	1.31	4.74×10^{-5}	0.9984	4.99×10^{-3}	0.03	0.49
Face B	2.98	7.50	2481	1.67	1.22	4.72×10^{-4}	-0.0036	4.83×10^{-3}	0.03	0.34

Table 2 Continued

Specimen identification	t (mm)	r_i (mm)	L (mm)	$ a_0 $ (mm)	$ c_3 $ (mm)	$2.54\sigma_{a_3}^2$ (mm)	δ/L (mm)	$\bar{\sigma}$ (mm)	ω_o ($\zeta = 1$) (mm)	ω_o ($\zeta = 10$) (mm)
PB 50×50×4 ($r_i = 3.5$)										
Face A	3.92	3.42	2475	3.22	2.50	4.28×10^{-6}	0.0000	2.37×10^{-3}	0.03	0.28
Face B	3.92	3.42	2481	3.06	2.38	1.75×10^{-5}	0.9980	2.46×10^{-3}	0.04	0.30
PB 50×50×4 ($r_i = 4.5$)										
Face A	3.92	4.25	2481	4.47	3.46	8.65×10^{-5}	0.9972	3.42×10^{-3}	0.02	0.25
Face B	3.92	4.25	2481	2.99	2.32	6.94×10^{-6}	0.0004	2.91×10^{-3}	0.02	0.08
PB 50×50×4 ($r_i = 7.5$)										
Face A	3.92	7.58	2475	4.12	3.26	2.16×10^{-5}	-0.0012	4.06×10^{-3}	0.02	0.24
Face B	3.92	7.58	2481	3.35	2.62	6.80×10^{-4}	0.0044	3.46×10^{-3}	0.02	0.10
PB 50×50×5 ($r_i = 3.5$)										
Face A	4.93	3.17	2488	4.21	3.22	5.71×10^{-4}	-0.0036	5.32×10^{-3}	0.03	0.13
Face B	4.93	3.17	2488	4.69	3.43	1.35×10^{-2}	0.0064	4.14×10^{-3}	0.04	0.39
PB 50×50×5 ($r_i = 4.5$)										
Face A	4.89	4.33	2495	4.48	3.41	1.41×10^{-3}	-0.0044	4.91×10^{-3}	0.02	0.19
Face B	4.89	4.33	2495	4.92	3.88	1.07×10^{-4}	-0.0032	2.93×10^{-3}	0.04	0.23
PB 50×50×5 ($r_i = 7.5$)										
Face A	4.90	7.50	2488	5.67	4.33	1.76×10^{-4}	0.9968	3.81×10^{-3}	0.05	0.15
Face B	4.90	7.50	2488	4.36	3.41	1.03×10^{-5}	-0.0008	3.23×10^{-3}	0.02	0.12
PB 50×50×6 ($r_i = 7.5$)										
Face A	6.03	7.50	2495	6.86	5.24	4.34×10^{-5}	0.9992	6.62×10^{-3}	0.05	0.25
Face B	6.03	7.50	2481	7.98	6.30	1.18×10^{-4}	-0.0020	6.38×10^{-3}	0.03	0.19

Table 3 Data for hot-rolled samples

Specimen identification	t (mm)	r_i (mm)	L (mm)	$ a_0 $ (mm)	$ c_3 $ (mm)	$2.54\sigma_{a_3}^2$ (mm)	δ/L (mm)	$\bar{\sigma}$ (mm)	ω_o ($\zeta = 1$) (mm)	ω_o ($\zeta = 10$) (mm)
HR 50×50×3										
Face A	3.00	4.54	5580	4.23	3.14	3.35×10^{-6}	-0.9996	1.80×10^{-3}	0.01	0.13
Face B	3.00	4.54	5593	7.41	5.38	7.57×10^{-5}	-0.0008	5.80×10^{-3}	0.01	0.13
HR 50×50×5										
Face A	4.95	4.50	5593	5.34	4.14	2.16×10^{-5}	0.0004	4.57×10^{-3}	0.05	0.42
Face B	4.95	4.50	5588	1.02	0.87	8.84×10^{-6}	-0.0004	2.92×10^{-3}	0.03	0.27
HR 50×50×6										
Face A	6.35	4.75	5593	1.87	1.30	8.87×10^{-6}	-0.9996	2.92×10^{-3}	0.01	0.13
Face B	6.35	4.75	5580	5.55	4.49	2.73×10^{-5}	-0.0008	3.49×10^{-3}	0.02	0.20
HR 50×50×10										
Face A	9.69	4.50	5593	19.27	15.03	2.06×10^{-4}	0.9992	9.56×10^{-3}	0.03	0.23
Face B	9.69	4.50	5600	22.90	17.56	4.64×10^{-5}	-0.0004	6.68×10^{-3}	0.02	0.16

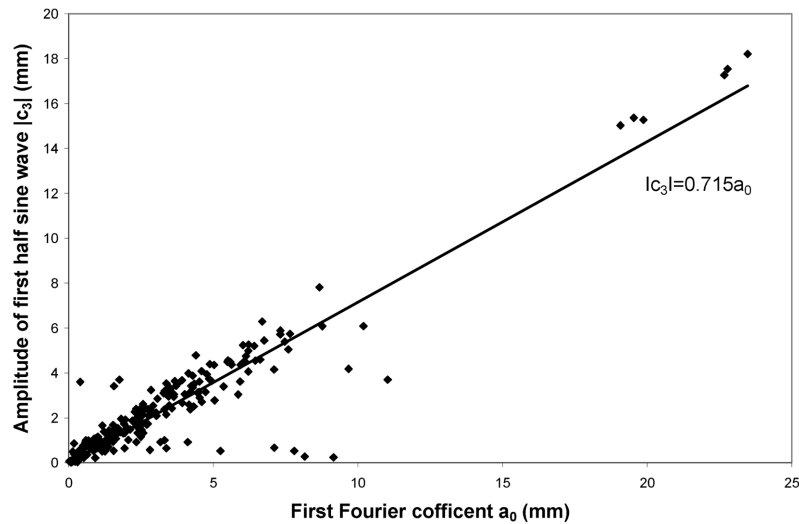


Fig. 15 Relationship between the first Fourier coefficient, a_0 and the amplitude of the first half sine wave, c_3 for the related data

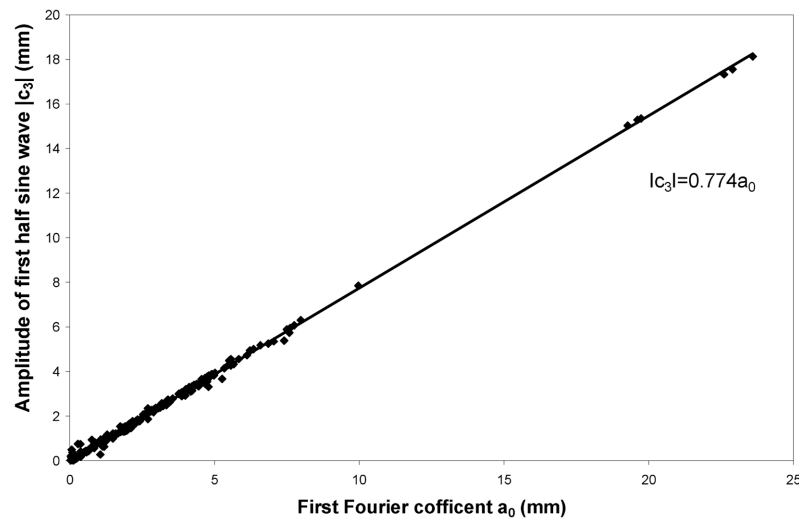


Fig. 16 Relationship between the first Fourier coefficient, a_0 and the amplitude of the first half sine wave, c_3 for the unrelated data

5. Results

Results from the Fourier and least squared spectral analyses are presented in Tables 1-3. The most significant peaks, according to the PRESS analysis for the least squared spectra was the first term of each series, with few exceptions. Figs. 15 and 16 show the correlation between the modulus of the first real (cosine) coefficient a_0 (which is identical to the first combined coefficient) of the Fourier transform and the modulus of the first half sine wave amplitude c_3 from the least squared technique.

Both relate to an overall bow in the specimens and are of a similar form to the buckled shape of an elastic pin-ended column.

By equating the area under a half sine wave with an amplitude of c_3 to the areas under a full cosine curve of amplitude a_0 it can be shown that there is a linear dependency, as stated by Eq. (25). This linear relationship is reflected in Figs. 15 and 16 by considering the slope of the linear regression curve. The unrelated data (where the three profiles on each face are analysed independently) shows an excellent correlation, whilst the increased scatter for the related profiles shows the effect of considering the imperfection profiles with respect to a common (surface) datum. It is therefore proposed that the first Fourier coefficient from a Fourier transform can be approximated to the amplitude of the half sine wave with the amplitude c_3 through Eq. (25) and this gives a good estimation of the global imperfection.

$$c_3 = \frac{\pi a_0}{4} \approx 0.785 a_0 \quad (25)$$

The least squared method of fitting a series of half sine waves to the imperfection function produces a function that is a very good fit to the experimental data, resulting in low covariance factors for the spectral peaks. The estimated experimental error is consistently lower than the actual experimental error, suggesting that the measurements were more accurate than predicted.

The modulus of the coefficient of the first half sine waves normalised against the specimen lengths L are plotted against their section thickness in Figs. 17 to 19. For the press-braked sections a clear trend of normalised global imperfections increasing with thickness is observed. A similar trend is observed for the hot-rolled sections, although more data would be required to confirm this relationship. The data presented does not however investigate any relationship that might exist between the global imperfection and the cross-section slenderness, as the width of section is constant for both press-braked and hot-rolled sections. The global imperfections for the cold-rolled sections showed no trend with thickness. Therefore, a half sine wave of amplitude c_3 , presented as a proportion of the member length L and determined from mean values, is proposed for representing global geometric imperfections for the three different forming processes (Eqs. (26) to (28)). Figs. 18

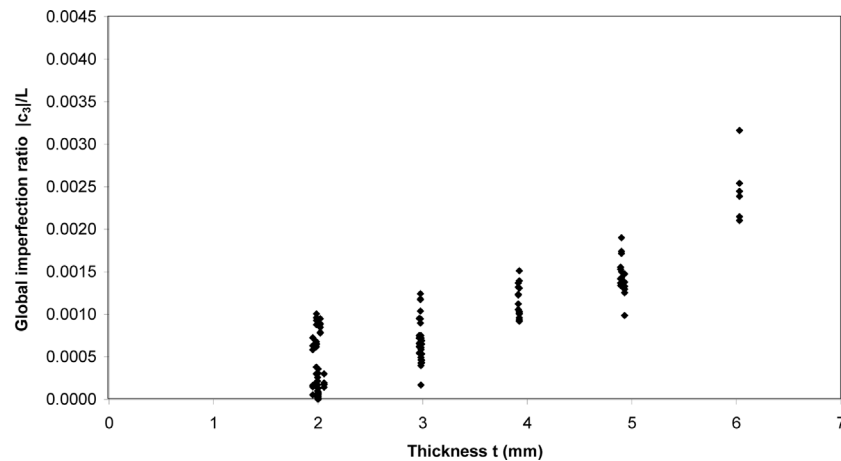


Fig. 17 Relationship between the normalised first half sine wave amplitude and the thickness of the section for press-braked sections (unrelated data)

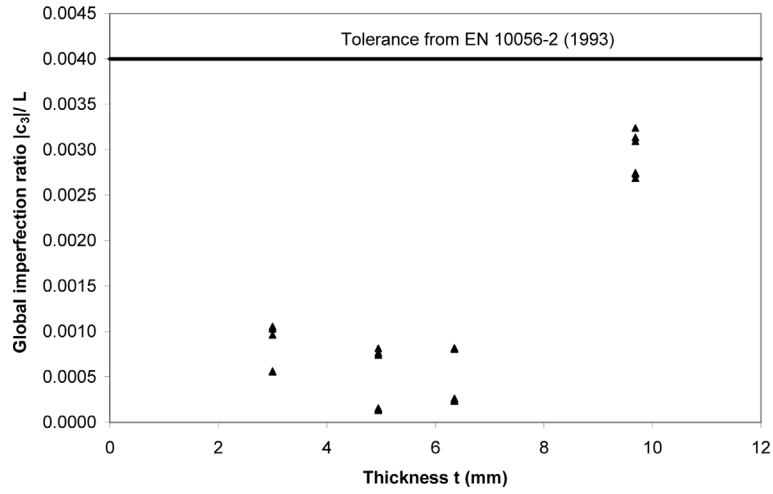


Fig. 18 Relationship between the first half sine wave amplitude and the thickness of the section for hot-rolled sections (unrelated data)

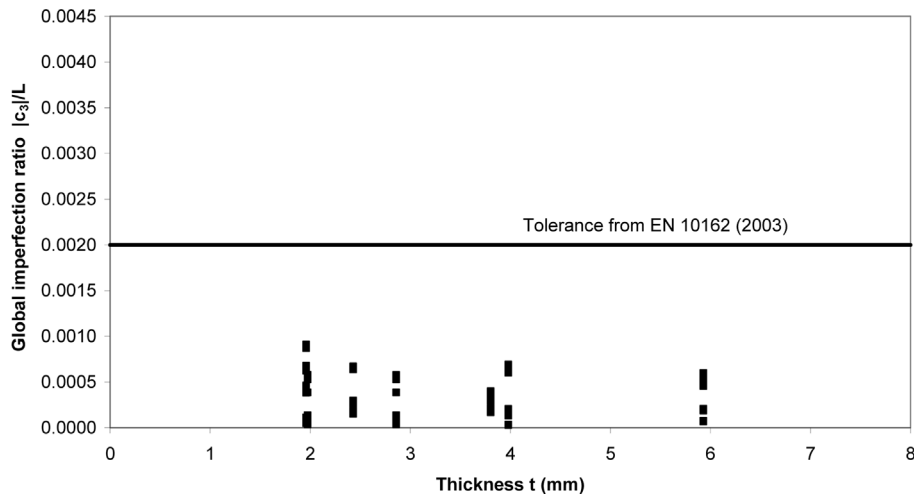


Fig. 19 Relationship between the first half sine wave amplitude and the thickness of the section for cold-rolled sections (unrelated data)

to 19 show that the global imperfections for cold-rolled sections and hot-rolled sections fall within their respective codes acceptable tolerances.

$$\text{Press-braked sections} \quad \frac{c_3}{L} \approx 0.00084 \quad (26)$$

$$\text{Hot-rolled sections} \quad \frac{c_3}{L} \approx 0.0012 \quad (27)$$

$$\text{Cold-rolled sections} \quad \frac{c_3}{L} \approx 0.00035 \quad (28)$$

Table 4 Data for cold-rolled samples

Specimen identification	t (mm)	r_i (mm)	L (mm)	$ a_0 $ (mm)	$ c_3 $ (mm)	$2.54\sigma_{a3}^2$ (mm)	δ/L (mm)	$\bar{\sigma}$ (mm)	$\frac{\omega_o}{(\zeta=1)}$ (mm)	$\frac{\omega_o}{(\zeta=10)}$ (mm)
CR 100×50×2										
Face A	1.98	2.31	5681	0.72	0.57	1.59×10^{-2}	0.9968	2.96×10^{-3}	0.02	0.30
Face B	1.98	2.31	5688	0.66	0.43	5.98×10^{-4}	-0.9980	3.29×10^{-3}	0.02	0.17
Face C	1.98	2.31	5695	3.76	3.00	1.31×10^{-5}	0.0004	3.56×10^{-3}	0.03	0.32
Face D	1.98	2.31	5681	4.13	3.30	6.35×10^{-5}	-0.0012	3.25×10^{-3}	0.03	0.14
CR 100×100×2										
Face A	1.96	2.94	5681	1.06	0.28	3.84×10^{-2}	0.0032	4.65×10^{-3}	0.07	0.54
Face B	1.96	2.94	5675	3.45	2.62	1.72×10^{-5}	-0.0004	4.08×10^{-3}	0.02	0.27
Face C	1.96	2.94	5675	4.97	3.85	6.56×10^{-4}	0.0020	3.46×10^{-3}	0.03	0.22
Face D	1.96	2.94	5675	6.35	5.00	4.10×10^{-5}	0.0008	4.31×10^{-3}	0.03	0.23
CR 100×50×3										
Face A	2.86	3.56	5695	0.72	0.57	1.59×10^{-2}	0.9968	2.96×10^{-3}	0.02	0.30
Face B	2.86	3.56	5695	0.66	0.43	5.98×10^{-4}	-0.9980	3.29×10^{-3}	0.03	0.17
Face C	2.86	3.56	5695	3.76	3.00	1.31×10^{-5}	0.0004	3.56×10^{-3}	0.03	0.32
Face D	2.86	3.56	5695	4.13	3.30	6.35×10^{-5}	-0.0012	3.25×10^{-3}	0.03	0.14
CR 100×100×3										
Face A	2.43	4.25	5681	1.07	0.95	8.20×10^{-5}	0.0012	3.69×10^{-3}	0.04	0.31
Face B	2.43	4.25	5688	1.47	1.06	4.43×10^{-4}	-0.0016	4.97×10^{-3}	0.05	0.36
Face C	2.43	4.25	5681	1.84	1.49	4.00×10^{-5}	-0.9992	4.24×10^{-3}	0.04	0.31
Face D	2.43	4.25	5681	4.56	3.66	1.78×10^{-4}	-0.9984	3.16×10^{-3}	0.04	0.36
CR 100×50×4										
Face A	3.98	1.93	5681	0.29	0.75	1.67×10^{-1}	-0.9964	5.41×10^{-3}	0.07	0.45
Face B	3.98	1.93	5695	1.61	1.18	7.93×10^{-4}	-0.0016	6.62×10^{-3}	0.04	0.09
Face C	3.98	1.93	5688	4.90	3.88	6.05×10^{-5}	0.0012	3.17×10^{-3}	0.02	0.28
Face D	3.98	1.93	5675	4.75	3.77	1.20×10^{-5}	1.0000	3.97×10^{-3}	0.02	0.07
CR 100×100×4										
Face A	3.81	2.27	5681	1.22	1.05	6.88×10^{-4}	-0.0024	1.98×10^{-3}	0.02	0.41
Face B	3.81	2.27	5681	1.30	1.16	3.04×10^{-3}	0.0024	4.17×10^{-3}	0.03	0.22
Face C	3.81	2.27	5675	2.08	1.66	3.52×10^{-6}	0.9996	1.85×10^{-3}	0.01	0.34
Face D	3.81	2.27	5688	2.54	2.08	3.38×10^{-5}	-0.0012	2.37×10^{-3}	0.02	0.30
CR 100×50×6										
Face A	5.93	4.75	5681	3.38	2.73	5.33×10^{-5}	-0.9988	2.98×10^{-3}	0.02	0.18
Face B	5.93	4.75	5681	0.58	0.37	4.97×10^{-6}	1.0000	2.55×10^{-3}	0.02	0.10
Face C	5.93	4.75	5681	1.33	1.09	3.85×10^{-6}	-0.9996	1.93×10^{-3}	0.01	0.25
Face D	5.93	4.75	5681	3.87	3.07	3.21×10^{-5}	0.0008	3.80×10^{-3}	0.01	0.14

The amplitudes of the local imperfections have been investigated by considering profile data taken along the flange tip for the angle sections and along the centreline of the faces of the box sections. In order to determine representative amplitudes for local imperfections the spectral peaks below a

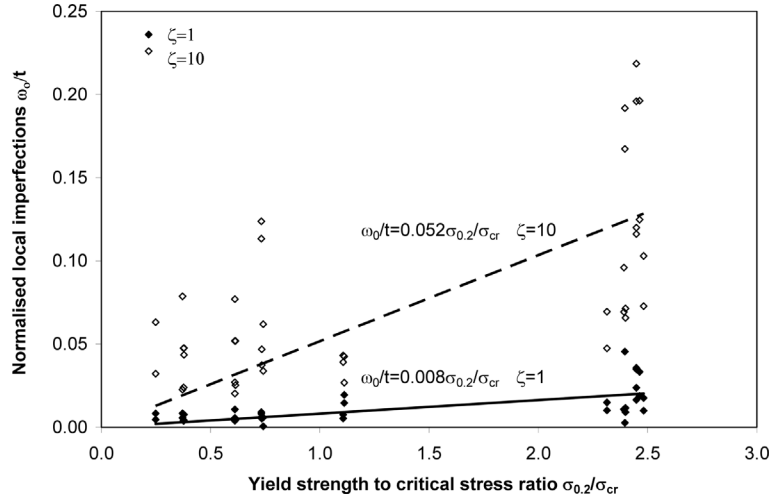


Fig. 20 Press-braked local imperfection normalised by thickness plotted against yield strength to critical stress ratio to determine α

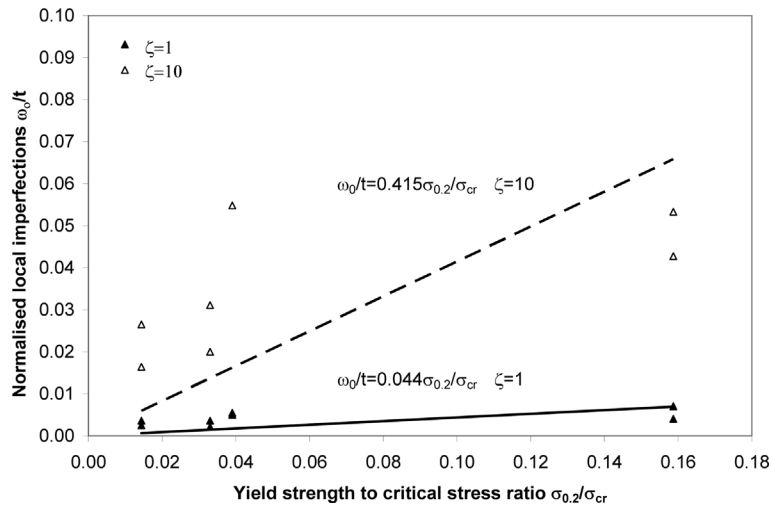


Fig. 21 Hot-rolled local imperfections normalised by thickness plotted against yield strength to critical stress ratio to determine α

specified frequency were assumed to relate to global imperfections and were removed. This frequency was defined in reference to a multiple ζ of the cross-section width; $\zeta = 1$ represents a half wavelength equal to the cross-section width, whilst $\zeta = 10$ represents a half wavelength of ten times the cross-section width. The remaining series was reformed as a profile of local imperfections and the maximum deviation from straightness ω_o was obtained. Values of this representative local imperfection are shown in the Tables 2 to 4, for the two cases of $\zeta = 1$ and $\zeta = 10$.

Figs. 20 to 22 plot the representative local imperfection amplitudes for $\zeta = 1$ and $\zeta = 10$ against the corresponding 0.2% proof stress (equivalent yield stress) to critical stress ratio ($\sigma_{0.2}/\sigma_{cr}$). A linear regression line passing through the origin has been determined for both sets of data to obtain values for α , as defined by the Dawson and Walker model of Eq. (2). It can be seen in Fig. 23 that

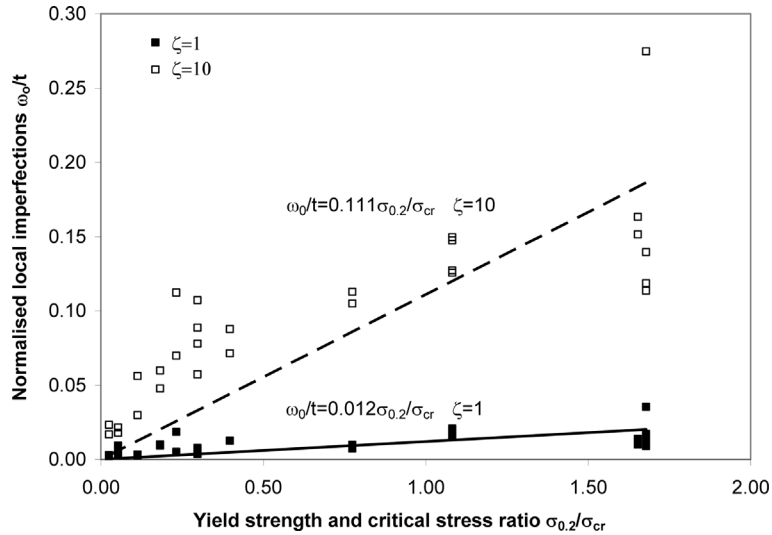


Fig. 22 Cold-rolled local imperfections normalised by thickness plotted against yield strength to critical stress ratio to determine α

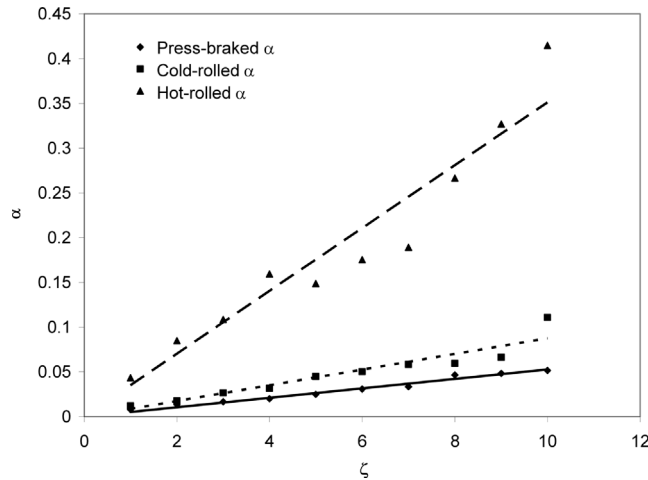


Fig. 23 Variation of α with ζ for the three different section types

α increases as ζ increases, which would be expected due to the inclusion of more low frequencies terms in the local imperfection profile which tend to be of larger amplitudes. Fig. 23 also shows the relative variation of α between the three production routes.

For the box sections, where the boundary conditions of the individual plate elements may be closely approximated as simply-supported, the half wavelength based on the elastic buckling mode (for practical aspect ratios) is equal to the plate width. This indicates that $\zeta = 1$ would provide the most suitable basis for determining local imperfection amplitudes. However, for outstand elements (one longitudinal edge simply-supported and one free), the half wavelength of the elastic buckling modes is equal to the length of the plate, though the failure mode localises due to post-buckling

Table 5 Upper and lower limits for values of α

	$\alpha (\zeta = 1)$	$\alpha (\zeta = 10)$
Press-braked equal angles	0.008	0.052
Hot-rolled equal angles	0.044	0.415
Cold-rolled SHS/RHS	0.012	0.111

behaviour and plasticity. It is therefore less straightforward to determine the most suitable value for ζ . It is reasonable to assume that the imperfection amplitudes corresponding to $\zeta = 1$ represent lower bound values whilst those corresponding to $\zeta = 10$ represent upper bound values. A summary of the proposed values of α to be used in Eq. (2) for the prediction of local imperfection amplitudes in structural stainless steel members is given in Table 5.

6. Conclusions

Structural stainless steel members are formed from a variety of production routes, which result in differing material properties, residual stresses and geometric imperfections. As part of a wider study, the magnitude and distribution of production related imperfections have been examined in this paper. An accurate method of measuring imperfections over long specimen lengths has been developed and implemented. Two analysis techniques, the classic Fourier transform and the least squared method fitting a series of half sine waves, have been employed to investigate the periodicity in the imperfections, from which the amplitudes of the global and local imperfections have been extracted. Simple predictive tools for both local and global imperfections have been developed to enable representative geometric imperfections for the three production processes (hot-rolling, cold-rolling and press-braking) to be incorporated into numerical models and design methods.

Acknowledgements

The authors would like to thank the structures technicians, Ron Millward and Alan Roberts at Imperial College London for the construction of the imperfection measurement rig and Corus RD & T, Swinden technology centre and Ancon for their technical expertise. The financial support of EPSRC and the Outokumpu Research Foundation is gratefully acknowledged.

References

- Bernard, E.S., Coleman, R. and Bridge, R.Q. (1999), "Measurement and assessment of geometric imperfections in thin walled panels", *Thin-Walled Structures*, **33**(2), 103-126.
- Berry, P.A., Rotter, J.M. and Bridge, R.Q. (2000), "Compression tests on cylinders with circumferential weld depressions", *J. Eng. Mech.*, ASCE, **126**(4), 405-413.
- Bracewell, R.N. (1986), *The Fourier Transform and Its Applications*, 2nd ed. McGraw-Hill International Editions.
- Chyssanthopoulos, M.K., Baker, M.J. and Dowling, P.J. (1991), "Statistical analysis of imperfections in stiffened cylinders", *J. Eng. Mech.*, ASCE, **117**(7), 1979-1997.
- Chyssanthopoulos, M.K. and Poggi, C. (1995), "Probabilistic imperfection sensitivity analysis of axially

- compressed composite cylinders”, *Eng. Struct.*, **17**(6), 398-406.
- Chou, S.M., Chai, G.B. and Ling, L. (2000), “Finite element technique for design of stub columns”, *Thin-Walled Structures*, **37**, 97-112.
- Dawson, R.G. and Walker, A.C. (1972), “Post-buckling of geometrically imperfect plates”, *J. Struct. Div.*, ASCE, **98**(ST1), 75-94.
- Ding, X., Colman, R. and Rotter, J.M. (1996), “Surface profiling system for measurement of engineering structures”, *J. Surveying Eng.*, ASCE, **122**(1), 3-14.
- Dubina, D. and Ungureanu, U. (2002), “Effect of imperfections on numerical simulation of instability behaviour of cold-formed steel members”, *Thin-Walled Structures*, **40**, 239-262.
- EN 10056-2 (1993), Specification for Structural Steel Equal and Unequal Leg Angles - Part 2: Tolerances on Shape and Dimensions, CEN.
- EN 10088-3 (2005), Stainless Steels - Part 3: Technical Delivery Conditions for Semi-finished Products, Bars, Rods and Sections for General Purpose, CEN.
- EN 10162 (2003), Cold Rolled Steel Sections - Technical Delivery Conditions - Dimensions and Cross-sectional Tolerances, CEN.
- Gardner, L. and Nethercot, D.A. (2004), “Numerical modelling of stainless steel structural components - A consistent approach”, *J. Eng. Mech.*, ASCE, **130**(10), 1586-1601.
- Gardner, L. (2005), “The use of stainless steel in structures”, *Progress in Structural Engineering and Materials*, **7**(2), 45-55.
- Haaland, D.M. and Thomas, E.V. (1988), “Partial least-squares methods for spectral analyses”, Relationship to other quantitative calibration methods and the extraction of qualitative information, *Analytical Chemistry*, **60**, 1193-1202.
- Hambly, E.T. and Calladine, C.R. (1996), “Buckling experiments on damaged cylindrical shells”, *Int. J. Solids Struct.*, **33**(24), 3539-3548.
- Hearne, G.E. and Metcalfe, A.V. (1995), *Spectral Analysis in Engineering Concepts and Cases*, Arnold publishers.
- Kaitila, O. (2002), “Imperfection sensitivity analysis of lipped channel columns at high temperatures”, *J. Constr. Steel Res.*, **58**, 333-351.
- Lechner, B. and Pircher, M. (2005), “Analysis of imperfection measurements of structural members”, *Thin-Walled Structures*, **43**, 351-374.
- Liu, Y. and Young, B. (2003), “Buckling of stainless steel square hollow section compression members”, *J. Constr. Steel Res.*, **59**, 165-177.
- Pacheco, L.A. and Durkin, S. (1988), “Denting and collapse of tubular members – A numerical and experimental study”, *Int. J. Mech. Sci.*, **50**(5), 317-331.
- Prenter, P.M. (1975), *Splines and Variational Methods*, John Wiley & Sons.
- Priestly, M.B. (1992), *Spectral Analysis and Time Series*, Academic press Ltd.
- Rasmussen, K.J.R. and Hancock, G.J. (1993), “Design of cold-formed stainless steel tubular members”, *J. Eng. Mech.*, ASCE, **119**(8), 2349-2367.
- Schafer, B.W. and Peköz, T. (1998), “Computational modelling of cold-formed steel: Characterizing geometric imperfections and residual stresses”, *J. Constr. Steel Res.*, **47**, 193-210.
- Singer, J. and Abramovich, H. (1995), “The development of shell imperfection measurement techniques”, *Thin-Walled Structures*, **23**, 379-398.
- Talja, A. and Salmi, P. (1995), “Design of stainless steel RHS beams, columns and beam-columns”, Research note:1619, VTT Building Technology, Finland.
- Teng, J.G., Lin, X., Rotter, J.M. and Ding, X.L. (2005), “Analysis of geometric imperfections in full-scale welded steel silos”, *Eng. Struct.*, **27**, 938-950.
- Trombka, J.I. and Schmadebeck, R.L. (1970), “A numerical least-squared technique for resolving complex pulse-height spectra”, In: Blackburn J.A. (1970), *Spectral Methods and Techniques*, New York, Marcel Dekker.
- Wheeler, A. and Pircher, M. (2002), “Measured imperfections in six thin walled steel tubes”, Research Report CCTR:001, Centre of Construction Technology and Research, University of Western Sydney.
- Wheeler, A. and Pircher, M. (2003), “Measured imperfections in six thin walled steel tubes”, *J. Constr. Steel Res.*, **59**, 1385-1395.

Notation

a_n	: cosine (real) Fourier coefficient or amplitude
$[A]$: design matrix
b_n	: sine (imaginary) Fourier coefficient or amplitude
b	: plate width
$\{c\}$: least squared coefficients in vector form
C	: column position
d	: plate width
$f_{CR}(x_m)$: profile created from located in column C and row R with imperfections from rig removed
$f_C(x_m)$: average profile created from column C imperfections from rig removed
$[G]$: weighting matrix
h	: concavity and convexity of internal elements
h'	: out of squareness for outstand elements
L	: member length
$laser_C$: laser reading aligned to a column position C
m	: location of discrete data point
M	: number of discrete data points
MA	: moving average
n	: Fourier number
N	: Nyquist frequency
$offset_{CR}$: offset value for transducer located in column C and row R
P_{CR}	: profile from column C and row R
$[Q]$: covariance matrix
r	: number of degrees of freedom
r_i	: internal corner radii of section
R	: row position
t	: member wall thickness
T_{CR}	: transducer reading located in column C and row R
$\{V\}$: modelling error
$\{w\}$: vector notation of imperfection function
x_m	: location along specimen length
x_1	: location of initial data point
\bar{x}_m	: normalised location along specimen length
α	: local imperfection coefficient as defined by Dawson and Walker (1972)
β	: local imperfection coefficient as defined by Dawson and Walker (1972)
δ	: offset of half sine wave series
ζ	: number of cross-section widths equal to half wavelength
σ_y	: yield stress
$\sigma_{0.2}$: 0.2% proof stress
σ_{cr}	: critical buckling stress
σ_m^2	: experimental variance in spectral coefficients
σ_{an}^2	: variance of least squared coefficients
$\hat{\sigma}_0^2$: variance factor
$\bar{\sigma}$: estimated experimental error
ω_o	: amplitude of local imperfections
ω_1	: amplitude of local imperfections in internal elements
ω_2	: amplitude of local imperfections in outstand elements